Journal of Cellular Physiology

RESEARCH ARTICLE

Telomere Attrition-Induced Senescence in Human Pluripotent Stem Cell-Derived Astrocytes: Distinct Cellular and Functional Characteristics

Dongyun Kim[1] | Seo Hyun Yoo[1] | Seung Soo Oh[1] | Gyu-Bum Yeon[1,2] | Jaeyeon Choi[1] | Jaewook Lee[1] | Sanghyun Park[3] | Dong-Wook Kim[3] | Dae-Sung Kim[1,2,4]

[1]Department of Biotechnology, College of Life Sciences and Biotechnology, Korea University, Seoul, Republic of Korea | [2]Institute of Animal Molecular Biotechnology, Korea University, Seoul, Seongbuk-gu, Republic of Korea | [3]Department of Physiology, Yonsei University College of Medicine, Seoul, Seodaemun-gu, Republic of Korea | [4]Department of Pediatrics, Korea University College of Medicine, Guro Hospital, Seoul, Guro-gu, Republic of Korea

Correspondence: Dong-Wook Kim (dwkim2@yuhs.ac) | Dae-Sung Kim (sonnet10@korea.ac.kr)

Received: 27 March 2025 | **Revised:** 23 November 2025 | **Accepted:** 25 November 2025

Funding: This study was supported by grants from the National Research Foundation of Korea (RS-2024-00344352), the Korean Fund for Regenerative Medicine (24A0101L1), and a research fund from Korea University.

Keywords: astrocytes | BIBR1532 | human pluripotent stem cells | reactive oxygen species | senescence | senescence-associated secretory phenotype | telomere attrition

ABSTRACT

This study explored the role of telomere attrition in astrocytic senescence by pharmacologically inhibiting telomerase activity in human induced pluripotent stem cell-derived astrocytes. Treatment with the telomerase inhibitor BIBR1532 (BIBR) during differentiation induced hallmark features of senescence, including nuclear lamina abnormalities, enhanced senescence-associated β-galactosidase activity, increased replication arrest and DNA damage, altered reactive oxygen species homeostasis in mitochondria, accompanied by significant shortening of relative telomere length. Despite these senescence related characteristics, BIBR-treated astrocytes exhibited limited changes in the expression of senescence-associated secretory phenotype-related genes. Moreover, their key functional properties, such as glutamate uptake, synaptic vesicle clearance, mitochondrial membrane potential and morphology remain comparable to those of control astrocytes. These findings suggest that the presence of classical senescence markers does not necessarily lead to functional impairment and that BIBR-induced senescence in astrocytes may represent an early or transitional phase, where classical senescence markers emerge without substantial functional decline. Our results reinforce the notion that while telomere attrition is a major cellular senescence driver, its onset may not be attributed to a single stressor but rather to a complex interplay of cellular stress pathways. This study provides valuable insights into the mechanisms underlying astrocytic senescence and underscores the need for further research on the molecular basis of its occurrence and functional implications.

1 | Introduction

Cellular senescence is a state of permanent cell cycle arrest triggered by various stressors including DNA damage, oxidative stress, and oncogenic signals. Initially identified as a tumor-suppressive mechanism in fibroblasts, senescence occurs in a wide range of cell types including neurons and glial cells of the central nervous system (CNS) (Zhang et al. 2024). In the CNS, cellular senescence

---

Dongyun Kim, Seo Hyun Yoo, and Seung Soo Oh contributed equally to this study.

© 2025 Wiley Periodicals LLC.

plays a crucial role in both normal aging and neurodegenerative disease progression. Aging is the primary risk factor for conditions such as Alzheimer's disease (AD), Parkinson's disease (PD), and amyotrophic lateral sclerosis, and understanding the contribution of senescent cells to neurodegeneration is important (Melo Dos Santos et al. 2024). CNS senescence is associated with neuroinflammation, reduced neural plasticity, and homeostatic disruption, which drive disease progression. Although the link between senescence and neurodegeneration is becoming clear, the precise molecular and cellular changes in senescent cells remain poorly understood, presenting challenges for developing targeted therapies.

Among the CNS cell types, astrocytes play a crucial role in maintaining homeostasis and supporting brain function; however, they also exhibit senescent phenotypes in the aging brain, which can contribute to neuroinflammation and neuronal dysfunction. Senescent astrocytes are characterized by DNA damage response (DDR) activation, mitochondrial dysfunction, and various pro-inflammatory cytokine release, known as the senescence-associated secretory phenotype (SASP). These factors promote chronic inflammation, which is a key driver of neurodegeneration in diseases such as AD and PD (Cohen and Torres 2019). Evidence from human postmortem studies and animal models indicates that senescent astrocytes accumulate in the aging brain and individuals with neurodegenerative diseases. Senescence markers such as $p16^{INK4a}$ and $p21^{Waf1/Cip1}$ are elevated in astrocytes from the brains of patients with AD and other neurodegenerative conditions (Baker and Petersen 2018). Additionally, the selective elimination of senescent astrocytes in a mouse model of AD improves cognitive function and reduces tau accumulation-associated pathological changes (Bussian et al. 2018). These findings suggest that targeting astrocyte senescence is a promising therapeutic approach for mitigating neurodegeneration. To clearly understand astrocyte senescence, researchers often employ in vitro cellular models using primary astrocyte cultures (Simmnacher et al. 2020). Exposing these cells to general stressors, such as oxidative stress or irradiation, induce senescence, allowing for the examination of changes in gene expression, secretory profiles, and cellular function (Boisvert et al. 2018). While these models have been instrumental in generating astrocytes with senescent phenotypes and examining the cellular pathways involved in senescence and the SASP, significant challenges remain in identifying the precise molecular pathways that drive senescence in the CNS and developing model systems that accurately replicate human pathology.

Cellular senescence is a complex process driven by the combined actions of various stresses and functional impairments, including telomere shortening, mitochondrial dysfunction, reactive oxygen species (ROS) imbalance, impaired proteostasis, and epigenetic alterations (Dodig et al. 2019; López-Otín et al. 2023). Of these, telomere shortening is a well-established driver of cellular senescence, particularly in proliferating cells, as critically short telomeres trigger DDR, activating pathways involving p53, $p21^{Waf1/Cip1}$, and $p16^{INK4a}$, ultimately leading to irreversible cell cycle arrest (Herbig et al. 2004). Telomerase, an enzyme that counteracts telomere shortening by extending telomere, exhibits cell-type specific roles in the CNS. While postmitotic neurons express the telomerase protein TERT for noncanonical functions like protection against oxidative stress (Lobanova et al. 2017; Spilsbury et al. 2015), astrocytes lack detectable telomerase activity. Consequently, astrocytes undergo pronounced telomere shortening with age (Tomita et al. 2018). Given these distinct mechanisms, modulating telomere length or telomerase activity, either by inhibition or gene disruption, in a cell-type specific manner represents a distinctive strategy for facilitating or studying cellular aging in the CNS. Previous studies using *Tert*-deficient mice (Jaskelioff et al. 2011), CRISPR–Cas9-mediated *TERT* knockout (Harley et al. 2024), and pharmacological telomerase inhibition (Vera et al. 2016) have provided clear evidence that telomere shortening drives senescence in CNS cells, including neurons and astrocytes.

Despite the established link between telomere shortening and senescence, critical questions remain regarding cellular aging in the CNS. Specifically, the extent to which telomere shortening contributes to cellular senescence and how broadly the cells exhibit senescence-related phenotypes remain key unresolved question. To address these issues, we used human induced pluripotent stem cells (hiPSCs) and a highly efficient differentiation method to generate functional astrocytes. We adopted a strategy involving the use of BIBR1532 (BIBR), a small-molecule telomerase inhibitor, to induce senescence. While BIBR is recognized for its proapoptotic properties at high concentrations, we employed a lower, non-cytotoxic dose and extended treatment regimen (Pascolo et al. 2002). This approach specifically utilizes its capacity as a selective telomerase inhibitor to induce progressive telomere attrition, thereby establishing a model of stable, replicative cellular senescence in astrocytes rather than acute cell death. We induced cellular senescence in hiPSC-derived astrocytes using a pharmacological telomerase inhibitor and systematically examined their molecular and functional characteristics.

2 | Materials and Methods

2.1 | Culture and Neural Differentiation of hiPSCs

A hiPSC line named NL1 was employed in this study (Yeon et al. 2023). The hiPSCs were cultivated on a 6-well plate coated with Matrigel (Corning, Corning, NY, USA) and maintained in StemMACS™ iPS-Brew XF medium (Miltenyi Biotec, Bergisch Gladbach, North Rhine-Westphalia, Germany). They were expanded through enzymatic passaging with 10 μM Y27632 (Millipore Sigma, St. Louis, MO, USA) treatment to prevent dissociation-induced cell death.

To differentiate hiPSCs into neural precursor cells (NPCs), the dual-SMAD inhibition method was employed as previously described with minor adjustments (Yeon et al. 2023). Briefly, hiPSCs were dissociated into individual cells, and 1×10^4 cells/cm^2 were plated on Matrigel-coated dishes in StemMACS iPS-Brew XF medium supplemented with 10 μM Y27632. On the initial day of differentiation, the cells were cultured in StemMACS™ iPS-Brew XF medium containing 500 nM LDN193189 (Selleck Chemicals, TX, USA) and 10 μM SB431542 (Millipore Sigma), maintaining this culture condition for 10 days. On day 10, the cells were dissociated with Accutase (Thermo Fisher Scientific) and resuspended in NPC medium [DMEM/F12 medium supplemented with 1× N2 and 1× B27, both sourced from Thermo Fisher Scientific, along with 20 ng/mL basic fibroblast growth factor (bFGF; Prospec, Ness-Ziona, Israel)]. Once more than 80% cell population tested positive for SOX1, a definitive marker of NPCs, these cells were classified as

10974652, 2025, 12, Downloaded from https://onlinelibrary.wiley.com/doi/10.1002/jcp.70118 by Yonsei University Med Library, Wiley Online Library on [22/01/2026]. See the Terms and Conditions (https://onlinelibrary.wiley.com/terms-and-conditions) on Wiley Online Library for rules of use; OA articles are governed by the applicable Creative Commons License

NPCs and subsequently employed for further differentiation into astrocytes or preserved by cryopreservation in liquid nitrogen for future use.

2.2 | Lentivirus Production

Plasmids carrying rtTA (Addgene catalog number 20342, MA, USA) or nuclear factor I B (NFIB) were introduced into 293 FT cells along with the packaging vectors pMDLg/pRRE, pRSV-Rev, and envelope pMD2.G (Addgene catalog numbers 12251, 1225, and 12,259, respectively) using Lipofectamine® 3000 (Thermo Fisher Scientific) following the manufacturer's instructions. The culture medium containing the viral components was harvested 72 h posttransfection and concentrated using a Lenti-X concentrator (Takara, Kusatsu, Japan). We also used an external service for large-scale virus production (VectorBuilder Inc., IL, USA). Upon titration, the concentrated viral particle suspension was divided into smaller portions and stored at −80°C for future use.

2.3 | Astrocyte Differentiation from NPCs

To initiate astrocytic differentiation from NPCs, a previously described protocol was used (Yeon et al. 2023). Briefly, 3×10^5 NPCs/cm^2 were seeded on a Matrigel-coated 6-well plate and cultured in NPC medium. The next day, the cells were exposed to viruses at 1.0 multiplicity of infection and 1 μg/mL polybrene in fresh NPC medium. To enhance the transduction efficiency, infection was conducted by centrifugation at 1000× g for 1 h at room temperature. After incubating for 18 h, the viral medium was replaced with fresh NPC medium containing 2.5 μg/mL doxycycline (DOX, Takara) to induce NFIB expression. The day on which DOX was added was counted as Day 0, and DOX was administered for 14 days. On the first day (Day 1), the medium was replaced with NPC medium devoid of bFGF but containing 10 ng/mL ciliary neurotrophic factor (CNTF) and 10 ng/mL bone morphogenetic protein 4 (BMP4) (both from PeproTech, Rocky Hill, NJ, USA). On Day 3, the medium was replaced with commercial astrocyte medium (ScienCell, CA, USA), which was continued until Day 14. The virus-infected cells were selected from Days 1 to 14 using 1.25 μg/mL puromycin (Thermo Fisher Scientific). On Day 14, 3×10^4 cells/cm^2 were transferred to Matrigel-coated 6- or 4-well plates and cultured in astrocyte maturation medium for another week. This medium was a 1:1 mixture of DMEM/F12 and Neurobasal medium supplemented with 1× N2, 1× GlutaMAX™ supplement (Thermo Fisher Scientific), 1 mM sodium pyruvate (Thermo Fisher Scientific), 5 μg/mL heparin-binding epidermal growth factor-like growth factor (PeproTech), 0.5 mg/mL dibutyryl-cAMP (MedChemExpress, NJ, USA), 5 μg/ml N-acetyl-L-cysteine (Millipore Sigma), 10 ng/mL BMP4, and 10 ng/mL CNTF.

2.4 | Telomerase Inhibition

BIBR1532 (#HY-17353) was purchased from MedChemExpress and diluted in dimethyl sulfoxide (DMSO; also used as the vehicle control) to produce a 10 mM stock solution, which was then stored at −80°C. BIBR1532 (final concentration: 10 μM after determining the optimal concentration) was freshly added every other day.

2.5 | Cell Viability Assay

Cell viability was assessed using the Chromo-CK™ Cell Viability Assay Kit (Monobio, Gyeonggi-do, Korea), following the manufacturer's guidelines. In brief, 10% of the total medium volume of the assay solution was added to each sample and incubated at 37°C for 1 h. Afterwards, the culture medium was transferred to a 96-well plate, and absorbance was measured at 450 nm with a Multi-Detection Microplate Reader (HIDEX, Turku, Finland).

2.6 | Senescence-Associated β-galactosidase Staining

Senescence-associated β-galactosidase (SA-β-gal) staining was conducted following a previously established method (Kohli et al. 2021). Briefly, the cells in a 4-well plate were washed twice with PBS. Subsequently, cells in each well were fixed with a solution of 2% paraformaldehyde and 0.2% glutaraldehyde in PBS for 5 min. Following fixation, 500 μL SA-β-gal staining solution [X-gal (Bioneer Inc, Daejeon, Korea) in 1 mg/mL dimethylformamide, 40 mM citric acid/sodium phosphate buffer (pH = 6.0), 5 mM potassium ferrocyanide, 5 mM potassium ferricyanide, 150 mM sodium chloride, and 2 mM magnesium chloride in water] was added to each well. The plate was sealed to prevent evaporation and incubated at 37°C for 12 h in a CO_2-free dry incubator. After rinsing the samples with PBS, they were incubated with 1 μg/mL 4′,6-diamidine-2′-phenylindole dihydrochloride (DAPI, Roche, Basel, Switzerland) in PBS for 5 min at room temperature to enable cell quantification. The images were captured using an inverted microscope (IX73) equipped with a digital camera (DP73; Olympus, Tokyo, Japan).

2.7 | Immunocytochemistry

The cells cultured in 4-well plates were fixed with 4% paraformaldehyde in PBS at room temperature for 15 min, washed with PBS, and permeabilized with 0.1% Triton X-100 in PBS for 10 min. Then, the cells were blocked using 2% bovine serum albumin in PBS for at least 1 h and incubated with primary antibodies overnight at 4°C. After thorough washing with PBS, the samples were incubated with appropriate secondary antibodies conjugated with fluorescent dyes (Alexa Fluor® 488 or 568; Thermo Fisher Scientific) at room temperature for 1 h. Finally, the cells were treated with 1 μg/mL DAPI in PBS for 5 min at room temperature to facilitate cell number quantification. Images were acquired using a fluorescence microscope (IX73) equipped with a digital camera (DP73). Primary antibodies used in this study were as follows: SOX1 (goat, 1:200; R&D Systems, Minneapolis, MN, USA), NESTIN (mouse, 1:200; Millipore Sigma), GFAP (rabbit, 1:1000; Dako, Glostrup, Denmark), S100β (mouse, 1:1000; Millipore Sigma), CD44 (rat, 1:100; Thermo Fisher Scientific), Lamin-B1 (LMNB1; rabbit, 1:1000; Abcam, Cambridge, UK), γH2AX (rabbit, 1:1000; Cell Signaling Technology), Ki67 (rabbit, 1:2000; Leica Biosystems, IL, USA), and C3 (mouse, 1:100; BioLegend, California, USA). Individual images for each channel corresponding to all merged-channel images are presented in Supplementary Figure 6.

10974652, 2025, 12, Downloaded from https://onlinelibrary.wiley.com/doi/10.1002/jcp.70118 by Yonsei University Med Library, Wiley Online Library on [22/01/2026]. See the Terms and Conditions (https://onlinelibrary.wiley.com/terms-and-conditions) on Wiley Online Library for rules of use; OA articles are governed by the applicable Creative Commons License

2.8 | Imaging Analysis

Astrocyte morphology was analyzed as described previously (Tavares et al. 2017). In summary, fluorescent images of S100β-labeled astrocytes were reconstructed and quantified using the Simple Neurite Tracer (SNT) plugin in ImageJ-Fiji (National Institutes of Health, MD, USA). The reconstruction process involved converting RGB images to 8-bit grayscale, followed by tracing S100β-positive astrocytic processes centered around DAPI-stained nuclei. Nuclear morphology analyses and LMNB1 and C3 intensity measurements were also performed using ImageJ Fiji. RGB images were converted to 8-bit grayscale, and the pixel intensities were segmented and measured using thresholding techniques.

2.9 | Cytokine Measurement

Cell culture supernatants were collected from astrocytes and analyzed using the LEGENDplex Human Inflammation Panel 1 (BioLegend) according to the manufacturer's instructions. Briefly, standards and cell culture supernatants were incubated with capture beads in 96-well V-bottom plates for 2 h. After washing, biotinylated detection antibodies were added to each well and incubated for 1 h, followed by streptavidin–phycoerythrin (PE) for 30 min. The samples were then resuspended in wash buffer and analyzed using flow cytometry (Agilent Technologies, California, USA).

2.10 | ROS Measurement

The total cellular ROS was measured using 2′,7′-dichlorodihydrofluorescein diacetate (H2DCFDA) (Thermo Fisher Scientific) following the manufacturer's instructions. Adherent cells were dissociated using Accutase and then resuspended. The suspended cells were subsequently exposed to H2DCFDA (final concentration: 10 μM) in astrocyte maturation medium at 37°C for 30 min. After incubation, the cells were washed once and resuspended in PBS for flow cytometric analysis using FACSymphony A1 (BD Biosciences). In total, 10,000 events were examined for each experimental condition. To evaluate mitochondrial ROS levels, MitoSOX™ Mitochondrial Superoxide Indicators (Thermo Fisher Scientific) were utilized. The suspended cells were incubated with MitoSOX™ (final concentration: 5 μM) in DPBS at 37°C for 15 min and analyzed using the same method.

2.11 | Lipid Droplet Analysis

The procedure for lipid droplet (LD) staining followed the same steps as those used for immunocytochemistry, including the blocking process. After blocking, the cells were stained with phalloidin (Thermo Fisher Scientific) for 45 min at room temperature according to the manufacturer's instructions. Following phalloidin staining, the cells were washed with PBS and then incubated with BODIPY 493/503 (final concentration: 1 μM, Thermo Fisher Scientific) in PBS at 37°C for 15 min.

2.12 | Mitochondrial Membrane Potential Measurement

JC-1 dye (MedChemExpress) was used to assess mitochondrial membrane potential (MMP). Briefly, the suspended cells were exposed to astrocyte maturation medium containing JC-1 (final concentration: 2 μM) and incubated at 37°C for 15 min. The cells were analyzed using the same flow cytometry method as described above.

2.13 | Mitochondrial Morphology Analysis

Mitochondrial morphology was analyzed using live cell images stained with MitoTracker^{TM} (Thermo Fisher Scientific) to visualize the mitochondria. The staining solution was prepared by adding a MitoTracker^{TM} probe (final concentration: 200 nM) to the astrocyte maturation medium. Cells cultured in a 4-well plate were washed, and pre-warmed (37°C) staining solution was added to the wells. After incubating at 37°C for 45 min, the cells were washed again, and fresh pre-warmed astrocyte maturation medium was added. Images were captured using a fluorescence microscope (IX73) equipped with a digital camera (DP73). The acquired images were then segmented at the cellular level and the mitochondrial network was quantified using the Mitochondria Analyzer plugin in ImageJ-Fiji.

2.14 | Glutamate Uptake Assay

At a given time point, astrocytes were thoroughly washed twice with HBSS (Thermo Fisher Scientific) and incubated in HBSS containing 100 μM glutamate for 2 h. Then, the media from the samples were collected and analyzed using a colorimetric glutamate assay kit (Abcam, Cambridge, UK) according to the manufacturer's instructions.

2.15 | Synaptosome Purification and in vitro Engulfment Assay

Synaptosomes were purified from mouse hippocampal tissues at postnatal day 1 using Syn-PER® Synaptic Protein Extraction Reagent (Thermo Fisher Scientific) and labeled with pHrodo™ Red Microscale Labeling Kit (Thermo Fisher Scientific) following the manufacturer's instructions. The astrocytes were cultured with 0.35 μL pHrodo-labeled synaptosomes. After 24 h, a minimum of five images per well were captured from random areas of the 4-well plate. The normalized area of pHrodo-labeled synaptosomes (fluorescent signal) was measured to calculate the extent of phagocytosis relative to the cell number.

2.16 | Telomere Length Measurement

DNA from astrocytes was extracted using the G-DEX™ IIc Genomic DNA Extraction Kit (iNtRON Biotechnology, Gyeonggi-do, Korea), following the provided manufacturer's guidelines. Telomere length was measured using a Relative Human Telomere Length Quantification qPCR Assay Kit (ScienCell) according to the manufacturer's instructions.

10974652, 2025, 12, Downloaded from https://onlinelibrary.wiley.com/doi/10.1002/jcp.70118 by Yonsei University Med Library, Wiley Online Library on [22/01/2026]. See the Terms and Conditions (https://onlinelibrary.wiley.com/terms-and-conditions) on Wiley Online Library for rules of use; OA articles are governed by the applicable Creative Commons License

A single-copy reference (SCR) primer set targeting a 100 bp segment of human chromosome 17 was used for data normalization. Quantification was achieved using the $2^{-\Delta Ct}$ method, where Ct represents the cycle value surpassing the detection threshold.

2.17 | RNA Isolation, Cdna Synthesis, and Real-Time PCR

TRIzol® (Thermo Fisher Scientific) was used to extract total RNA according to the manufacturer's instructions. For complementary DNA (cDNA) synthesis, 1 µg total RNA was used with the PrimeScript® RT Master Mix (Takara). Subsequently, quantitative PCR (qPCR) was conducted using the Fast SYBR® Green Master Mix (Thermo Fisher Scientific) on the StepOnePlus® Real-Time PCR System (Thermo Fisher Scientific). The primer sequences used in this study are listed in the Supplementary Table.

2.18 | Western blot Analysis

Astrocyte lysates were prepared using RIPA lysis buffer supplemented with a protease and phosphatase inhibitor cocktail. Equal amounts of protein (25 µg) were loaded on an 8% Bis-Tris gel, separated in NuPAGE MES buffer (Thermo Fisher Scientific), and transferred to polyvinylidene fluoride (PVDF) membranes (Millipore Sigma) using a Mini-PROTEAN III apparatus (Bio-Rad). The primary antibodies used were anti-p16^{INK4a} (mouse, 1:1000; Thermo Fisher Scientific), anti- p21$^{Waf1/Cip1}$ (mouse, 1:1000; Santa Cruz Biotechnology, TX, USA), anti-GATA4 (rabbit, 1:100; Santa Cruz Biotechnology), anti-p53 (mouse, 1:1000; Santa Cruz Biotechnology), anti-phospho-p53 (Ser15) (rabbit, 1:1000; Cell Signaling) and anti-β-actin (mouse, 1:1000; Santa Cruz Biotechnology). The secondary antibody used was horseradish peroxidase (HRP)-conjugated anti-mouse immunoglobulin G (1:2000; Cell Signaling Technology). Protein bands were detected using enhanced chemiluminescence reagent (Thermo Fisher Scientific).

2.19 | Cell Cycle Analysis

Adherent cells were detached using Accutase (Thermo Fisher Scientific), collected, and pelleted by centrifugation. The pellet was fixed overnight at −20°C with 70% ethanol. Fixed cells were then stained for 1 h at room temperature in DPBS containing 50 µg/ml propidium iodide. After a wash, flow cytometric analysis was performed using a FACSymphony A1 cytometer (BD Biosciences).

2.20 | NF-κB Reporter Assay

A set of reporter lentiviruses was used to monitor the NF-κB-regulated signaling pathway. These lentiviral reporters contain a fluorescent EGFP reporter under the control of a minimal CMV promoter (mCMV), embedded with four tandem repeats of the NF-κB transcriptional response element (NF-κB-TRE) sequence motif (5′-GGGACTTTCC). EGFP expression was analyzed by flow cytometry using FACSymphony A1.

2.21 | Statistical Analysis

Experiments were conducted in triplicate or more, and the data are presented as the mean ± standard error of the mean. Normality was determined using the Shapiro–Wilk test for samples with $n < 30$ and the Kolmogorov–Smirnov test for samples with $n \geq 30$. Normally distributed data were analyzed using Student's *t*-test for comparisons between two groups or one-way analysis of variance followed by Tukey's post-hoc test for comparisons involving more than two groups. Non-normally distributed data were analyzed using the Mann–Whitney U test for comparisons between two groups or the Kruskal–Wallis test of variance, followed by Dunn's post-hoc test for comparisons involving more than two groups. Statistical significance was set at $p < 0.05$.

3 | Results

3.1 | BIBR Treatment Induces Senescence-Like Morphological Changes in hiPSC-Derived Astrocytes

In this study, we aimed to induce senescent astrocytes from hiPSCs using the telomerase inhibitor, BIBR. To achieve this, determining the optimal concentration and appropriate temporal window for application is essential. Our astrocyte differentiation protocol involved generating NPCs from hiPSCs. Since astrocytes naturally exhibit low or negligible telomerase activity (Spilsbury et al. 2015), we first tested the timing of BIBR treatment within the initial 10 days of NPC differentiation where the cells are actively proliferative and applied 10–40 µM BIBR (Supplementary Figure 1A). Treatment with up to 20 µM BIBR did not impair NPC induction, as indicated by the number of NESTIN- and SOX1-positive cells (Supplementary Figure 1B–D). However, higher concentrations (> 40 µM) significantly reduced the yield of marker-positive cells and negatively impacted cell viability compared to lower concentrations (Supplementary Figure 1B–D). Moreover, 40 µM BIBR-treated cells exhibited significantly flattened soma with large and irregular nuclei (Supplementary Figure 1B, E–F), suggesting that the surviving cells had already entered cellular senescence. Additionally, exposure to 20 µM BIBR for 10 days and beyond also affected cell viability (Supplementary Figure 1G), with morphological alteration resembling those treated with 40 µM (data not shown). Based on these findings, we determined that 10 µM BIBR was the optimal concentration for use in subsequent differentiation experiments.

We previously demonstrated that overexpression of nuclear factor IB (NFIB), a transcription factor essential for gliogenesis, promotes the efficient and rapid differentiation of NPCs into functional astrocytes (Yeon et al. 2021). To induce senescent astrocytes in BIBR-treated NPCs, we overexpressed NFIB using a lentiviral delivery system. As we previously observed that one-fifth of the NPC population remained proliferative for 2 weeks following NFIB transduction (Yeon et al. 2021) (Figure 2D), BIBR treatment was maintained from the NPC stage through day 14 of astrocyte differentiation (Figure 1A). On Day 21 of astrocyte differentiation, the cells were stained with antibodies against astrocyte markers, including S100β, GFAP, and CD44. The results indicated that BIBR treatment did not affect astrocyte differentiation efficiency. In both the vehicle-treated control and BIBR-treated groups, over 90% cells

10974652, 2025, 12, Downloaded from https://onlinelibrary.wiley.com/doi/10.1002/jcp.70118 by Yonsei University Med Library, Wiley Online Library on [22/01/2026]. See the Terms and Conditions (https://onlinelibrary.wiley.com/terms-and-conditions) on Wiley Online Library for rules of use; OA articles are governed by the applicable Creative Commons License

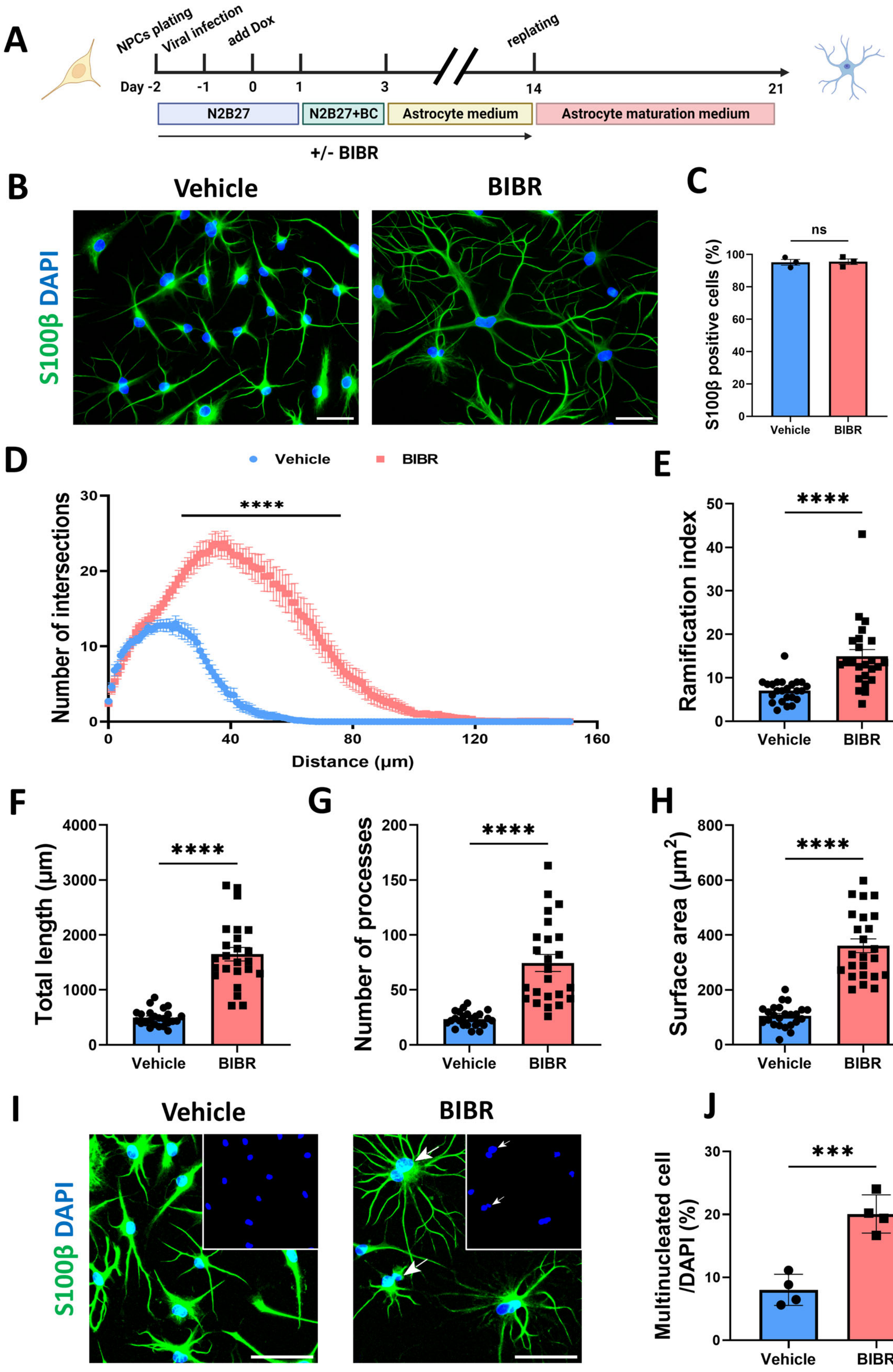

FIGURE 1 | Legend on next page.

10974652, 2025, 12, Downloaded from https://onlinelibrary.wiley.com/doi/10.1002/jcp.70118 by Yonsei University Med Library, Wiley Online Library on [22/01/2026]. See the Terms and Conditions (https://onlinelibrary.wiley.com/terms-and-conditions) on Wiley Online Library for rules of use; OA articles are governed by the applicable Creative Commons License

were positive for all tested markers, with no statistically significant difference between the groups (Figure 1B–C, Supplementary Figure 2). However, a striking difference was observed in the cell morphology. Astrocytes in the BIBR-treated group had significantly large and flattened cell bodies, with highly branched and elongated processes (Figure 1B, D–H) and often multiple nuclei, a phenomenon referred to as multinucleation (Figure 1I–J), which are considered key morphological characteristics of senescent cells (Kloc et al. 2022).

3.2 | Senescence-Associated Molecular Changes in BIBR-Treated Astrocytes

Encouraged by the observed morphological changes, we proceeded with molecular characterization of astrocytes. SA-β-gal staining, a cytochemical technique that is used to identify senescent cells, revealed that BIBR treatment significantly increased the number of SA-β-gal-positive cells compared to vehicle-treated control condition (29.91 ± 1.27 for control group vs. 51.32 ± 2.047 for BIBR-treated group; Figure 2A–B). Interestingly, the number of SA-β-gal-positive cells in the BIBR-treated group did not significantly increase with extended culture (by Day 33), whereas the control group showed a continued upward trend (Supplementary Figure 3). This suggests that BIBR treatment may induce premature senescence rather than accelerate the natural process toward senescence. Therefore, most of the subsequent cellular and functional assessments were conducted on Day 21.

We observed an approximately 50% reduction in relative telomere length in astrocytes derived from BIBR-treated NPCs compared to those from vehicle-treated controls (Figure 2C). Furthermore, the BIBR-treated group was significantly less proliferative as indicated by approximately half of the number of KI67-positive cells compared with control group (20.71 ± 0.84 for control group vs. 9.96 ± 0.53 for BIBR-treated group; Figure 2D), indicating that BIBR treatment promoted cell cycle exit and a shift toward a postmitotic state in more cells. Previous studies have shown that critically short telomeres can be recognized as damaged DNA, triggering cellular pathways involved in the DDR and often leading to cell cycle arrest or senescence (Hewitt et al. 2012). Consistently, the BIBR-treated group exhibited significantly more nuclei with γH2AX immunoreactivity, a well-established DNA damage marker (Mah et al. 2010) (Figure 2E). Defects of nuclear lamina, a structural protein network in the nucleus, are associated with cellular senescence (Kim 2023). In particular, reduced Lamin-B1 (LMNB1), a key component of the nuclear lamina, along with impaired nuclear integrity is considered a hallmark of senescent astrocytes (Matias et al. 2022). Recent studies have linked altered LMNB1 levels to defects in DDR, suggesting that LMNB1 loss contributes to age-related cellular dysfunction (Etourneaud et al. 2021). In line with these results, immunofluorescent staining for LMNB1 showed reduced immunoreactivity in the BIBR-treated group, accompanied by significantly larger and less spherical nuclei compared to the control group (Figure 2F–I). Finally, lipid droplet (LD) build-up within a cell is closely linked to cellular senescence and is recognized as a biomarker for senescent cells (Maestri et al. 2024). To assess this, we measured the LD levels in astrocytes using BODIPY lipid staining. Our results revealed significantly more BODIPY-positive cells in BIBR-treated astrocytes than in controls, indicating pronounced LD accumulation (Figure 2J–K). These findings further support the notion that telomere attrition induces cellular senescence in hiPSC-derived astrocytes.

3.3 | Molecular Characterization of BIBR-Treated Senescent Astrocytes

$p21^{Waf1/Cip1}$, also known as cyclin-dependent kinase inhibitor1 (CDKN1A), is a critical regulator of cell cycle arrest, and its high levels are a canonical hallmark of senescent cells responding to DNA damage and stress signals (Yan et al. 2024). Our western blot analysis analysis of the BIBR-treated group showed a significant increase in $p21^{Waf1/Cip1}$ protein levels (Figure 3A–B), strongly supporting the senescence phenotype observed thus far. To further elucidate the underlying mechanism, we investigated the key cell cycle regulators $p16^{INK4a}$ and p53 throughout the differentiation period. BIBR treatment resulted in a significant increase in both total p53 and phosphorylated p53−Ser15 levels (Figure 3C–E). The phosphorylation of p53 at Ser15 is a critical upstream event that stabilizes and activates p53, leading to its ability to induce $p21^{Waf1/Cip1}$ transcription and subsequent cell cycle arrest (Kumari and Jat 2021). In contrast, there was no detectable difference in $p16^{INK4a}$ protein levels between the BIBR-treated and control groups (Figure 3C and F). This distinct pattern suggests that the BIBR-induced senescent phenotype operates through a p53-dependent mechanism. Consistent with these molecular findings, cell cycle analysis further confirmed the functional outcome: BIBR treatment induced an instant and significant increase in the G1 phase population and a corresponding decrease in the S/G2 − M phase population at an early stage (Day 0-7), compared with non-treated control cells (Supplementary Figure 4). It is important to note that, regardless of the BIBR treatment, we observed an elevated baseline p53 level in the early stage of differentiation compared to the later stage (Day 14–21). This is consistent with previous reports that p53 levels are elevated during initial astrocyte differentiation to promote astrogliogenesis (Liu et al. 2013). Furthermore, a transient increase of $p16^{INK4a}$ on Day 7 was also observed, which we attribute to the NFIB overexpression actively driving the necessary cell cycle arrest for commitment to the astrocyte lineage (Yeon et al. 2021).

FIGURE 1 | Morphological and quantitative analysis of astrocytes. (A) Schematic illustration of the differentiation protocol for astrocytes with and without BIBR treatment. N2B27: the culture medium containing N2 and B27 supplements; BC: BMP4 and CNTF. (B) Representative immunofluorescence images of vehicle- and BIBR-treated astrocytes stained for S100β. Scale bar: 50 μm. Images were acquired using a 20× objective (200× total magnification). (C) Quantification of S100β-positive cells under each condition. Quantification was made with 15 fluorescent images from three independent differentiation batches. Each dot represents the mean percentage of positive cells in each batch. (D–H) Morphological assessments using Sholl analysis. (D) The number of intersections was quantified as a function of distance from the cell body to assess astrocyte ramification. Based on the results, ramification index (E), total dendritic length (F), number of processes (G), and surface area (H) were analyzed. (I) Representative images of astrocytes and DAPI-stained nuclei (insets) in control and BIBR-treated groups. Images were captured using a 20× objective. White arrows indicate multinucleated cells and their nuclei. Scale bars: 50 μm. (J) Quantification of multinucleated astrocytes under each condition. ns: not significant, $^{***}p < 0.001$, and $^{****}p < 0.0001$.

10974652, 2025, 12, Downloaded from https://onlinelibrary.wiley.com/doi/10.1002/jcp.70118 by Yonsei University Med Library, Wiley Online Library on [22/01/2026]. See the Terms and Conditions (https://onlinelibrary.wiley.com/terms-and-conditions) on Wiley Online Library for rules of use; OA articles are governed by the applicable Creative Commons License

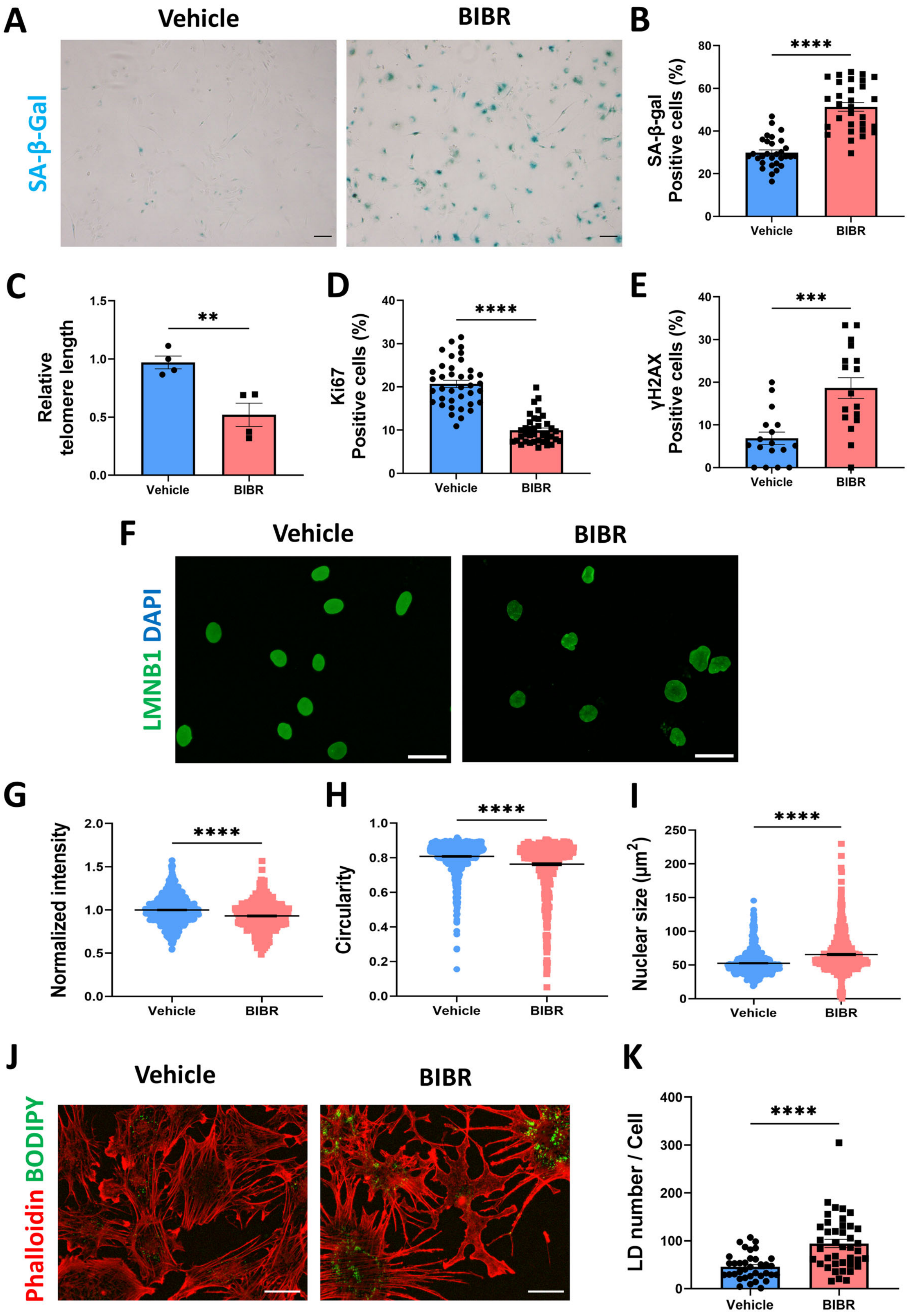

FIGURE 2 | Legend on next page.

10974652, 2025, 12, Downloaded from https://onlinelibrary.wiley.com/doi/10.1002/jcp.70118 by Yonsei University Med Library, Wiley Online Library on [22/01/2026]. See the Terms and Conditions (https://onlinelibrary.wiley.com/terms-and-conditions) on Wiley Online Library for rules of use; OA articles are governed by the applicable Creative Commons License

The combined molecular and functional data strongly support that BIBR treatment facilitates astrocytic senescence in a p53–p21$^{Waf1/Cip1}$-dependent manner, rather than the p16^{INK4a}-mediated pathway.

3.4 | Involvement of Reactive Oxygen Species and Mitochondria in BIBR-mediated astrocytic Senescence

Next, we explored the possibility that other cellular stressors, such as oxidative stress, were involved in the observed cell cycle arrest, as ROS, a major source of oxidative stress in the cell, are key contributors to DNA damage and cellular senescence (Borodkina et al. 2014). When measuring the total ROS level using the fluorescent dye H2DCFDA, we observed no significant differences between the two astrocyte groups (Figure 4A). We then investigated mitochondrial ROS (mtROS). Labeling with MitoSOX™, a mitochondrial superoxide indicator, showed a significant increase in mtROS levels in astrocytes from the BIBR-treated group compared to those from the controls (Figure 4B). To further investigate the implication of increased mtROS without a corresponding rise in total cellular ROS, we assessed mitochondrial function and structure by measuring mitochondrial membrane potential (MMP) and mitochondrial morphology. As a result, we observed no significant changes in either MMP or morphology between the two groups (Figure 4C, D–E). This lack of change in overall mitochondrial integrity suggests that the electron transport chain had not undergone a widespread collapse. Instead, the increased mtROS production likely stems from a localized or specific imbalance (e.g., a defect in Complex I or III) (Bleier et al. 2015). This specific increase could represent localized 'hotspots' of ROS production that act as a stress signal, propagating to the nucleus to activate the observed senescence pathways (Nousis et al. 2023). While the localized mtROS increase is probable, it remains unclear whether this specific mitochondrial stress is the primary driver of the senescence pathway or if it is a secondary consequence of the cellular senescence already induced by the BIBR-mediated telomere shortening. The precise upstream mechanism linking BIBR to mtROS production warrants further in-depth investigation.

3.5 | Function Assessments Revealed Minimal Impairments in BIBR-treated senescent Astrocytes

Previous studies have shown that senescent astrocytes exhibit various functional impairments, including reduced ability to support neurons, clear neurotransmitters, and synaptic debris (Cohen and Torres 2019; Kim et al. 2024). These deficits are often accompanied by the SASP, which collectively contributes to neurodegenerative diseases. Interestingly, our functional assessments revealed no significant impairments in the BIBR-treated group regarding their ability to take up excitatory neurotransmitters (such as glutamate) or remove synaptic debris (Figure 5A–B). When analyzing the expression of inflammatory cytokines (*IL-1α, IL-1β, IL-6, IL-8*) and chemokine (*CCL2*), we observed an interesting pattern: *IL-1α*, *IL-1β*, and *CCL2* mRNA levels were upregulated in the BIBR-treated group than in the controls, whereas *IL-6* and *IL-8* mRNA levels remained unchanged (Figure 5C). However, when we examined protein levels using a bead-based multiplex immunoassay, IL-1α and IL-1β proteins were undetectable in both groups (data not shown), while CCL2 protein level was elevated in the BIBR-treated group (Figure 5F). In contrast, IL-6 and IL-8 protein levels remained unchanged or were even higher in control astrocytes (Figure 5D–E). The lack of upregulation of IL-6 and IL-8 proteins, along with increased *IL-1α* and *IL-1β* mRNA levels without corresponding protein production, suggests possible incomplete SASP activation. To further investigate this, we examined the NF-κB signaling pathway, a key regulator of SASP (Salminen et al. 2012), using an NF-κB reporter assay. Under baseline conditions, astrocytes in the BIBR-treated group showed mildly elevated NF-κB activity compared to controls, but this difference was not statistically significant, consistent with the expression of SASP genes. Interestingly, when stimulated by IL-1β treatment, astrocytes in BIBR-treated group exhibited significantly higher NF-κB activity and a corresponding increase in *IL-6* and *IL-8* expression than control cells (Figure 5G and Supplementary Figure 5). These findings suggest that although BIBR-treated astrocytes are not fully pro-inflammatory, they are primed for an enhanced inflammatory response when exposed to external inflammatory cues. A previous study found that the SASP is induced by preventing the autophagy-mediated degradation of the transcription factor GATA4 (Kang et al. 2015). Normally, GATA4 is selectively degraded through autophagy; however, it accumulates in senescent cells and activates NF-κB, driving SASP, independent of the p53–p16^{INK4a} pathway. We found that GATA4 protein levels remained unchanged in astrocytes from the BIBR-treated group and controls (Figure 5H–I). This finding aligns with the results for SASP gene expression and NF-κB activity, verifying that the signaling pathways driving SASP are not fully activated. Taken together, the minimal SASP characteristics, along with the preserved ability to take up neurotransmitters and clear synaptic debris, suggest that these cells are not fully committed to senescence or may be in their early stages, as indicated in a previous study (Oguma et al. 2023).

FIGURE 2 | Characterization of Cellular Senescence Phenotypes. (A, B) The culture treated with BIBR showed an increased proportion of senescence-associated β-galactosidase-positive cells compared to the vehicle-treated astrocyte culture. A total of ten random microscopic fields were captured and quantified from each group across three independent differentiation batches. Scale bar: 50 μm. Images were captured using a 10× objective. (C) The relative telomere length of control and BIBR-treated astrocytes. Data was obtained from four batches of differentiation. (D, E) Quantification of Ki67- and γH2AX-positive cells. Immunofluorescent images ($n = 38$ for Ki67; $n = 17$ for γH2AX) were utilized for quantification, derived from four independent differentiation experiments. (F) Representative immunofluorescence images of LMNB1 in astrocytes for each group. Scale bar: 20 μm. Images were captured using a 20× objective. (G–I) Quantification and comparison of astrocyte nuclear morphology between vehicle and BIBR groups. Each dot represents a value measured in a single cell. Quantification was performed using at least 10 immunofluorescent images captured per group from three independent differentiation batches. (J) Representative images of LDs (BODIPY 493/503, green) in astrocytes, with cytoplasm defined by Phalloidin-labeled actin filaments (red). Scale bar, 20 μm. Images were captured using a 40× objective. (K) Quantification of LD-containing cells. Immunofluorescence images ($n = 36$ for control; $n = 41$ for BIBR group) obtained from three batches of differentiation, were used for quantification. Each dot represents the mean value measured in each image. $^{**}p < 0.01$, $^{***}p < 0.001$, $^{****}p < 0.0001$.

10974652, 2025, 12, Downloaded from https://onlinelibrary.wiley.com/doi/10.1002/jcp.70118 by Yonsei University Med Library, Wiley Online Library on [22/01/2026]. See the Terms and Conditions (https://onlinelibrary.wiley.com/terms-and-conditions) on Wiley Online Library for rules of use; OA articles are governed by the applicable Creative Commons License

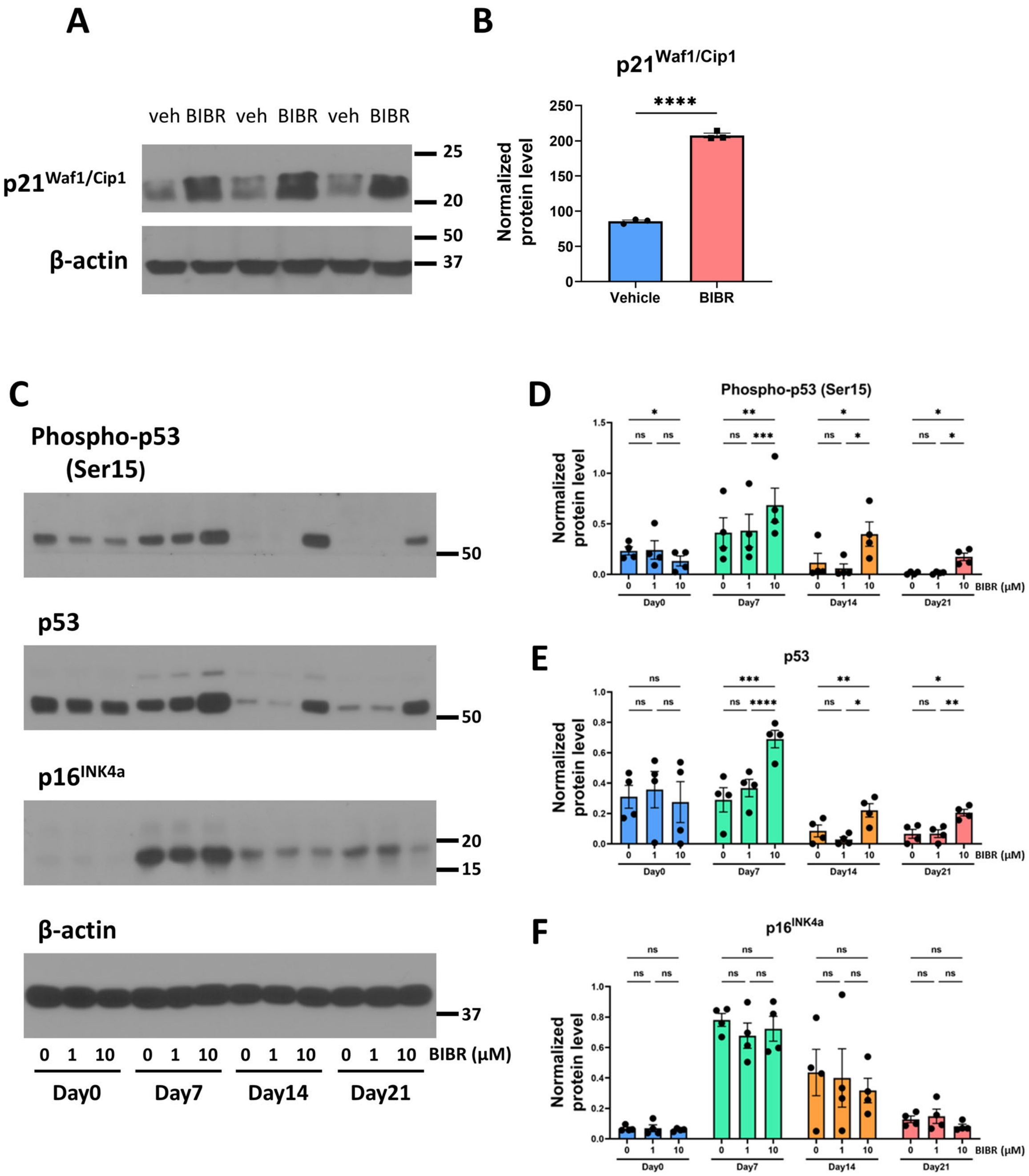

FIGURE 3 | Analysis of protein levels involved in the senescence mechanism. (A) Western blot shows the increased p21$^{Waf1/Cip1}$ protein level in BIBR-treated astrocytes compared with vehicle-treated astrocytes. (B) Quantification of p21$^{Waf1/Cip1}$ protein levels normalized to β-actin. (C) Western blot analysis of phospho-p53 (Ser15), p53, p16^{INK4a}, and β-actin in astrocytes treated with vehicle (0 μM), 1 μM, or 10 μM BIBR at different time points (Day 0, 7, 14, and 21). (D–F) Quantification of protein levels normalized to β-actin: phospho-p53 (Ser15) (D), total p53 (E), and p16^{INK4a} (F). ns: not significant, *$p < 0.05$, **$p < 0.01$, ***$p < 0.001$, and ****$p < 0.0001$.

3.6 | Expression of Reactive Markers Were Upregulated In BIBR-Treated Senescent Astrocytes

Previous studies have demonstrated that astrocytes isolated from aged mice upregulated a set of genes characteristic of "A1-type" reactive astrocytes (Boisvert et al. 2018; Clarke et al. 2018). This suggests that astrocytes may adopt a "reactive" phenotype during normal aging, contributing to neuroinflammation and exacerbating neurodegenerative processes. To investigate whether astrocytes derived from BIBR-treated NPCs exhibited similar reactive characteristics, we examined the expression of A1-type marker genes (Liddelow et al. 2017). Our results showed a significant upregulation of the mRNA levels of several A1-type marker genes, including *LCN2*, *C3*, and *C4B* (Figure 6A–C). Immunocytochemistry followed by image-based quantification further confirmed the increased number of C3-positive cells in the BIBR-treated group than in the control group (Figure 6D–E). Notably, this reactive gene expression pattern emerged in the absence of extrinsic stimuli, such as TNF-α, IL-1α, and C1q, the inflammatory cocktail known to

10974652, 2025, 12, Downloaded from https://onlinelibrary.wiley.com/doi/10.1002/jcp.70118 by Yonsei University Med Library, Wiley Online Library on [22/01/2026]. See the Terms and Conditions (https://onlinelibrary.wiley.com/terms-and-conditions) on Wiley Online Library for rules of use; OA articles are governed by the applicable Creative Commons License

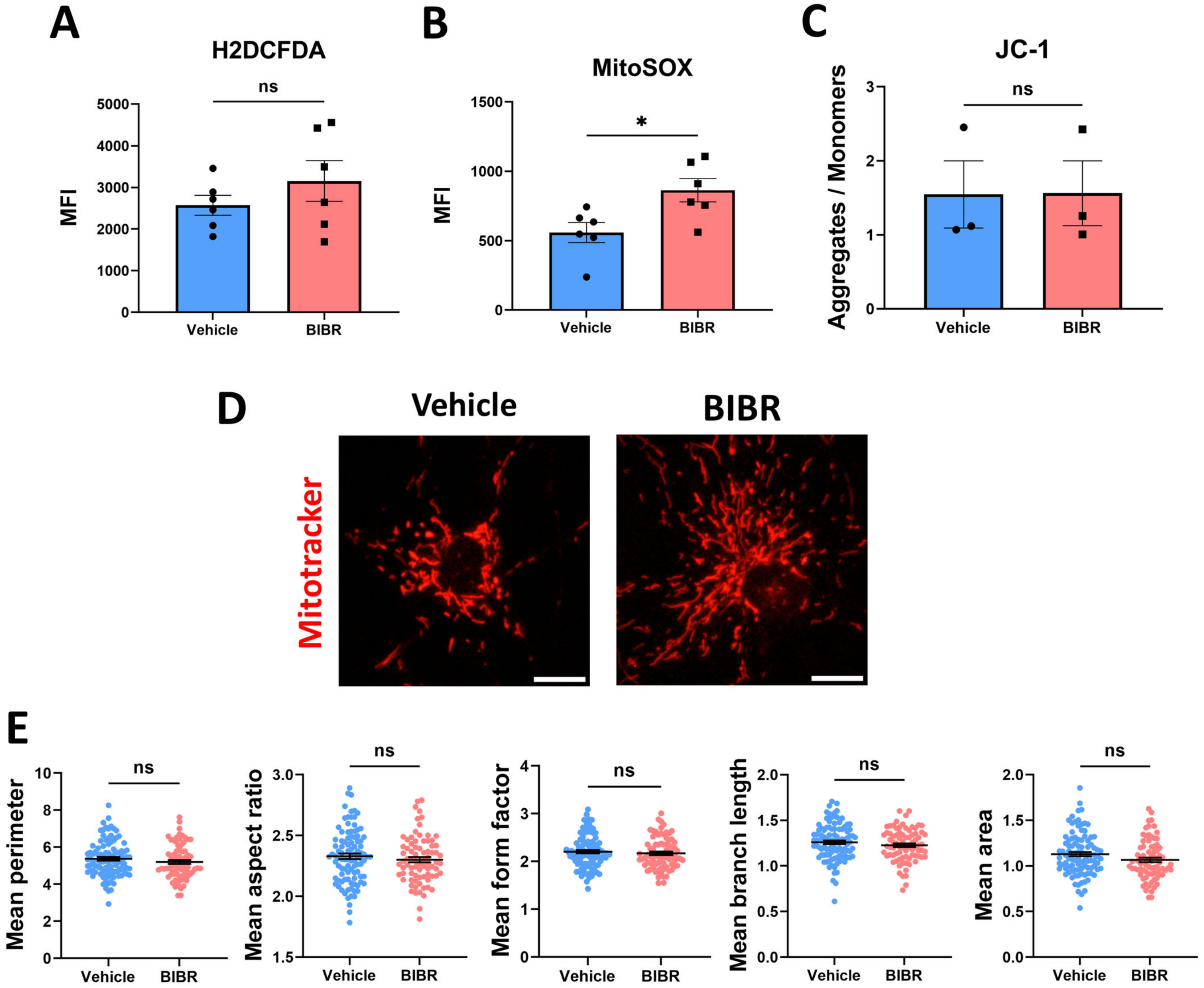

FIGURE 4 | Assessment of ROS and mitochondrial involvement in senescence of astrocytes following BIBR treatment. (A, B) Total cellular and mitochondrial ROS measurement in astrocytes using H2DCFDA and MitoSOX™. (C) Measurement of MMP in astrocytes using JC-1. Each dot represents the value measured from independent batches of differentiation (n = 6 for (A) and (B); n = 3 for (C)). MFI: mean fluorescence intensity. (D) Representative images of astrocytes showing mitochondria labeled with MitoTracker^{TM}. Scale bar, 10 μm. Images were captured using a 40× objective. (E) Comparison and quantification of mitochondrial morphology between control and BIBR-treated astrocytes. Mean perimeter: average mitochondrial boundary length; mean aspect ratio: length-to-width ratio indicating elongation; mean form factor: shape complexity; mean branch length: average length of mitochondrial network branches; and mean area: average mitochondrial size. ns: not significant and $*p < 0.05$.

induce 'A1-type' reactivity (Liddelow et al. 2017). This suggests that the observed phenotypical changes were likely intrinsic, possibly driven by alterations in molecular pathways within astrocytes following BIBR-treatment. Interestingly, although A1-type marker genes were upregulated, SASP-related genes exhibited only mild changes. This may be explained by a previous study suggesting that senescent astrocytes display distinct gene expression patterns compared to reactive astrocytes, particularly in pathways related to DDR and mechanistic target of rapamycin (mTOR) (Simmnacher et al. 2020), which is crucial for inflammatory cytokine protein levels. Collectively, the BIBR-treated astrocytes exhibit reactive astrocyte traits similar to those of senescent astrocytes, but lack clear signs of the SASP. Further studies are needed to determine whether this represents a unique astrocytic state or a transitional phase toward full senescence.

4 | Discussion

This study demonstrated that pharmacological inhibition of telomerase activity during differentiation can induce cellular senescence in hiPSC-derived astrocytes. Astrocytes exposed to the telomerase inhibitor, BIBR, throughout differentiation exhibited key features of senescent cells, including nuclear shape abnormalities, reduced LMNB1 level, and increased SA-β-gal activity. Compared with their untreated counterparts, the treated cells displayed several characteristics of replicative senescence: a shortening of relative telomere length, an increased number of cells undergoing cell cycle arrest, frequent signs of DNA damage, and elevated mtROS levels. These findings collectively indicate that telomerase inhibition facilitates replicative senescence. However, this senescent phenotype was incomplete. Specifically, changes in the expression of SASP-related genes were limited, though BIBR-treated astrocytes

10974652, 2025, 12, Downloaded from https://onlinelibrary.wiley.com/doi/10.1002/jcp.70118 by Yonsei University Med Library, Wiley Online Library on [22/01/2026]. See the Terms and Conditions (https://onlinelibrary.wiley.com/terms-and-conditions) on Wiley Online Library for rules of use; OA articles are governed by the applicable Creative Commons License

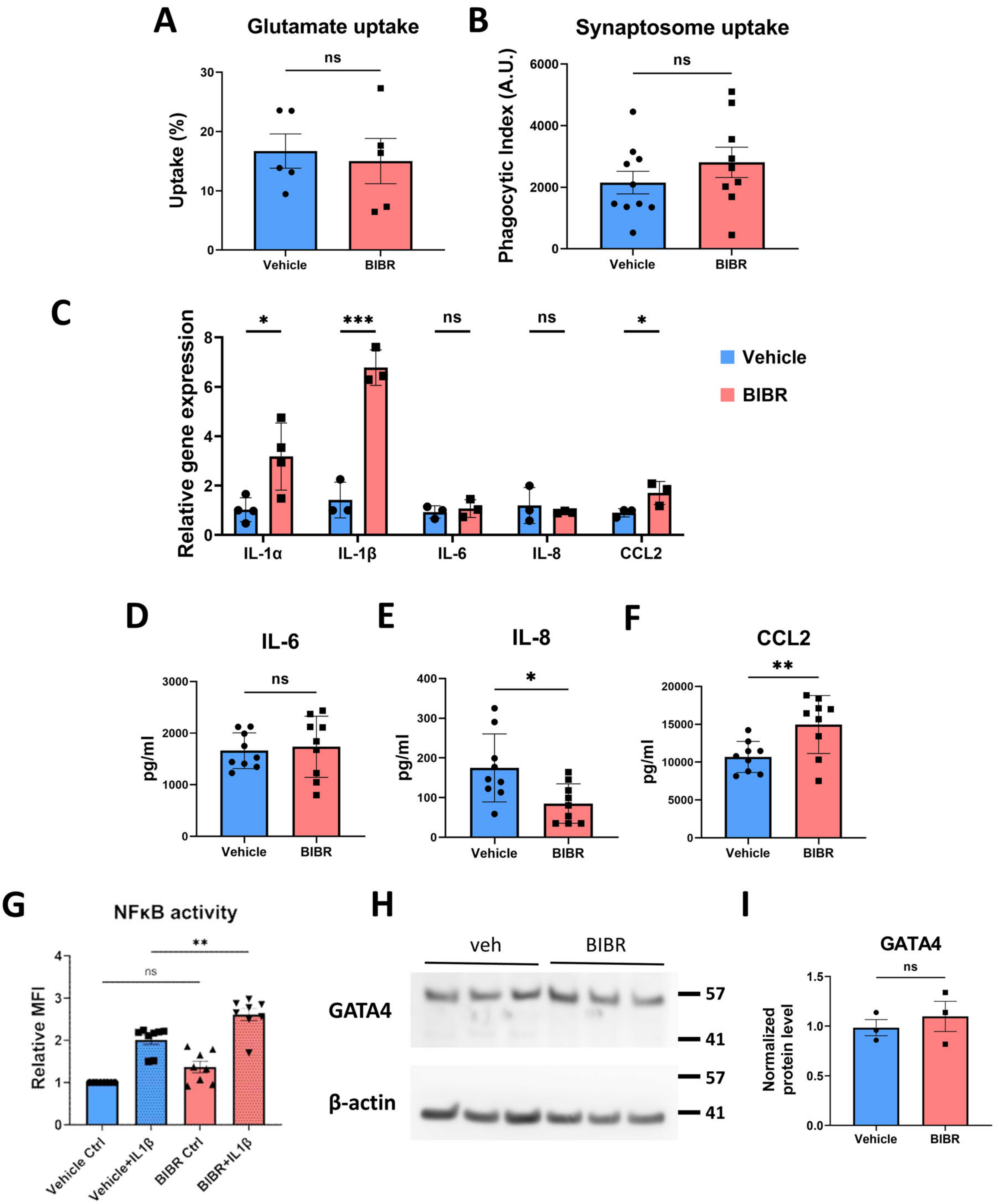

FIGURE 5 | Minimal senescence-associated functional impairment in BIBR-treated astrocytes. (A) The glutamate uptake assay revealed no significant difference between vehicle and BIBR-treated astrocytes. Data was obtained from five independent batches. (B) The synaptosome uptake assay using a pHrodo-Red indicator revealed no significant difference between vehicle and BIBR-treated astrocytes. Each dot represents the value from an individual image, obtained across three independent experiments. A.U.: arbitrary unit. (C) Quantitative gene expression analysis for various SASP genes. Data was obtained from more than three batches of differentiation. (D–F) Cytokine concentrations in the supernatant of vehicle and BIBR-treated astrocytes. Data were acquired from three independent differentiation batches. Each dot represents the value of three technical replicates within a single batch. (G) NF-κB transcriptional activity measured by a reporter system expressing EGFP under four tandem repeats of the NF-κB-TRE sequence motif. To measure NF-κB transcriptional activity in the stimulated state, the cells in each group were treated with 20 ng/mL IL-1β for 24 h. MFI: mean fluorescence intensity. (H) GATA4 protein level between vehicle and BIBR-treated astrocytes. (I) Normalized quantification of GATA4 protein level shown in (H). No significant difference was observed between two groups. ns: not significant, *$p < 0.05$, **$p < 0.01$, and ***$p < 0.001$.

10974652, 2025, 12, Downloaded from https://onlinelibrary.wiley.com/doi/10.1002/jcp.70118 by Yonsei University Med Library, Wiley Online Library on [22/01/2026]. See the Terms and Conditions (https://onlinelibrary.wiley.com/terms-and-conditions) on Wiley Online Library for rules of use; OA articles are governed by the applicable Creative Commons License

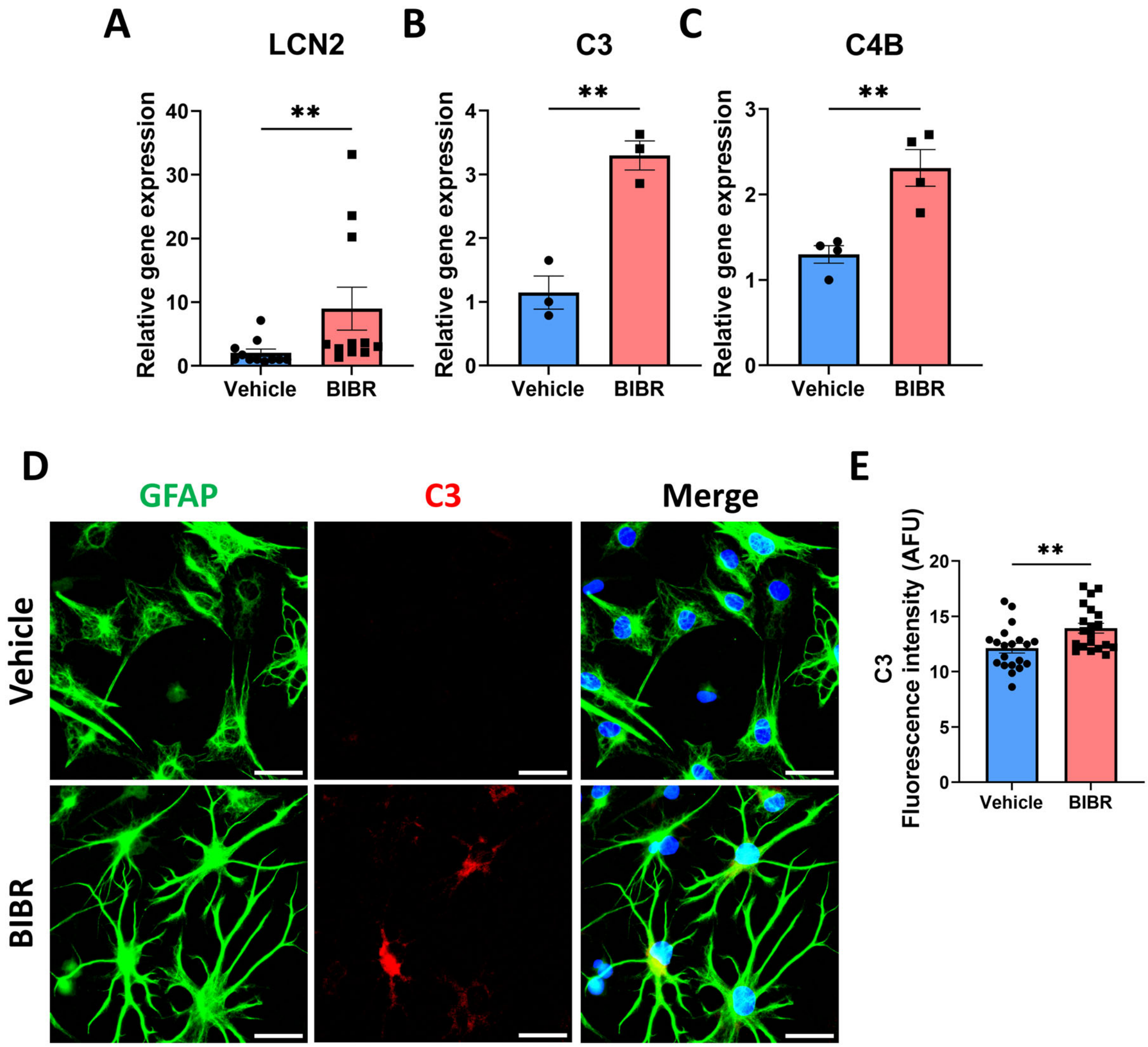

FIGURE 6 | Increased expression of reactive astrocyte makers in BIBR-treated cells. (A–C) Quantitative gene expression analysis for reactive astrocyte marker genes. (D) Representative immunofluorescence images of C3 in astrocytes. Scale bar: 20 μm. Images were captured using a 40× objective. (E) Quantification of C3 fluorescence intensity under each condition. Each dot represents the mean intensity per field (n = 5 fields per batch) derived from an independent batch of differentiation (n = 4 batches). AFU, arbitrary fluorescence unit. $^{**}p < 0.01$.

did exhibit an enhanced pro-inflammatory response upon stimulation. Moreover, their ability to uptake glutamate and clear synaptic vesicles as well as their MMP and overall mitochondrial morphology remained comparable to control astrocytes. These findings suggest that the presence of classical senescence phenotypes does not necessarily lead to functional impairment. While BIBR-treated astrocytes exhibit classical senescent traits, they do not yet show functional impairments, possibly indicating an early or transitional stage of senescence.

In our previous study, prolonging the astrocyte culture for an additional 3 weeks after the initial differentiation using the identical differentiation paradigm rapidly induced a broad spectrum of senescence-associated phenotypes (Kim et al. 2024). These senescent cells exhibited extensive DNA damage, mitochondrial dysfunction with elevated ROS, dysregulated lipid metabolism, and increased SASP. This severe senescence was accompanied with a ~35% reduction in relative telomere length. Given the absence of an external stimulus, this telomere shortening was likely driven by the cumulative effects of cellular stress caused by the prolonged in vitro cultivation. In the present work, however, we directly inhibited telomerase activity using BIBR during the astrocyte differentiation. This treatment caused an even more pronounced 50% reduction in relative telomere length, a decrease greater than that observed with prolonged culture. However, interpreting this portion is complicated because the BIBR treatment coincided with lentivirus-mediated NFIB overexpression, and this viral infection itself could have acted as an additional stressor contributing to telomere shortening and senescence (Baz-Martínez et al. 2016; Chuprin et al. 2013; Lee et al. 2021). Interestingly, despite the greater reduction in relative telomere length (50% vs. 35%), the BIBR-treated cells exhibited milder senescence-related phenotypes overall compared to those induced by prolonged cultivation. This result also supports the notion that while pharmacologically inhibiting telomerase activity is a strategy that drives astrocyte senescence, this approach alone is not sufficient to fully induce the comprehensive senescent state. These mild senescence phenotypes raise two important questions: Is pharmacological telomerase inhibition an inherently

10974652, 2025, 12, Downloaded from https://onlinelibrary.wiley.com/doi/10.1002/jcp.70118 by Yonsei University Med Library, Wiley Online Library on [22/01/2026]. See the Terms and Conditions (https://onlinelibrary.wiley.com/terms-and-conditions) on Wiley Online Library for rules of use; OA articles are governed by the applicable Creative Commons License

inefficient method for inducing cellular senescence? Alternatively, is telomere attrition alone insufficient to trigger senescence in neural lineage cells?

A previous study by Vera et al. demonstrated that pharmacological inhibition of telomerase can induce age-related phenotypes in neurons. In that study, human embryonic stem cells (hESCs) were treated with BIBR at concentrations ranging from 10 to 40 μM, starting 2 weeks before differentiation and continuing for 18 days during differentiation into dopaminergic neurons. Notably, treatment with 10 μM BIBR—the same concentration used in our study—resulted in only "modest" telomere shortening, yet was sufficient to induce phenotypes associated with aging and neurodegenerative diseases in the resulting neurons (Vera et al. 2016). These findings support the intriguing concept that telomere shortening can serve as a cue for inducing senescence during the differentiation of hESCs into neural lineage cells. On the other hand, a more recent study by Harley et al. employed CRISPR–Cas9 to knock out the gene encoding the key telomerase subunit *TERT* in hiPSCs. This genetic approach led to a 58%–61% reduction in telomere length. Upon differentiation, the resulting neurons and astrocytes exhibited various senescence-related characteristics, including reduced proliferation, upregulation of $\text{p21}^{\text{Waf1/Cip1}}$, increased DNA damage, and altered soma size. Transcriptomic analysis further revealed the upregulation of stress-related and inflammatory genes (Harley et al. 2024). Taken together, these findings suggest that, regardless of the experimental approach used, telomere shortening in human pluripotent stem cells (hPSCs) contributes to the emergence of premature senescence phenotypes in both differentiated neurons and astrocytes. Nonetheless, several factors must be considered when evaluating the effectiveness of telomere shortening as a means to induce cellular senescence across studies. These include differences in methods used to measure telomere length, the types of stem cells employed (hESCs vs. hiPSCs), the differentiated cell types studied (neurons vs. astrocytes), and the experimental approaches used to assess senescence phenotypes. Given the complex and heterogeneous nature of senescence (Sacco et al. 2021), its identification and characterization require multifaceted approaches, with careful consideration of the specific cellular context. In this context, when utilizing pharmacological telomerase inhibition, caution is necessary during the interpretation of results, as the effects of small-molecule inhibitors can vary significantly depending on their concentration and treatment duration and may also produce off-target effects beyond their intended mechanism. Furthermore, the selection of the method used to quantify telomere shortening warrants additional scrutiny. Our PCR-based quantification is rapid but only yields relative telomere length, not absolute length. Since cellular senescence is known to be induced specifically by critically short telomeres, more precise quantitative approaches, such as terminal restriction fragment analysis or quantitative fluorescence in situ hybridization, would provide more accurate and informative data on the extent of telomere shortening. Additionally, our investigation into telomere shortening and its role in cellular senescence was conducted within the specific context of hiPSC differentiation into astrocytes following a particular differentiation protocol. Therefore, these findings may not apply to other biological systems. Nevertheless, our results reinforce the idea that while telomere attrition is a crucial driver of cellular senescence, senescence is unlikely to be triggered by a single stressor. Instead, it appears to arise from the complex interplay between interdependent cellular stress pathways. Lastly, it is noteworthy that senescence can be induced not only by critically short telomeres, but also by telomeric damage—especially in post-mitotic cells that do not undergo telomere shortening—and can occur entirely independently of telomeres, as seen in stress-induced premature senescence and oncogene-induced senescence (Di Micco et al. 2021). Despite these diverse triggers, they share common upstream regulators and downstream hallmarks.

Author Contributions

Dongyun Kim, Seo Hyun Yoo, and Seung Soo Oh designed and performed the experiments, analyzed and interpreted the data, and wrote the manuscript. Gyu-Bum Yeon, Jaeyeon Choi, Jaewook Lee, and Sanghyun Park performed the experiments, and analyzed and interpreted the data. Dong-Wook Kim provided funding and experimental materials, and reviewed and edited the manuscript. Dae-Sung Kim conceived and designed the experiments, supervised the project, wrote the manuscript, and approved the manuscript for publication.

Conflicts of Interest

The authors declare no conflicts of interest.

Data Availability Statement

The data that support the findings of this study are available in the supporting material of this article.

References

Baker, D. J., and R. C. Petersen. 2018. "Cellular Senescence in Brain Aging and Neurodegenerative Diseases: Evidence and Perspectives." *Journal of Clinical Investigation* 128, no. 4: 1208–1216. https://doi.org/10.1172/JCI95145.

Baz-Martínez, M., S. Da silva-Álvarez, E. Rodríguez, et al. 2016. "Cell Senescence Is An Antiviral Defense Mechanism." *Scientific Reports* 6: 37007. https://doi.org/10.1038/srep37007.

Bleier, L., I. Wittig, H. Heide, M. Steger, U. Brandt, and S. Dröse. 2015. "Generator-Specific Targets of Mitochondrial Reactive Oxygen Species." *Free Radical Biology and Medicine* 78: 1–10. https://doi.org/10.1016/j.freeradbiomed.2014.10.511.

Boisvert, M. M., G. A. Erikson, M. N. Shokhirev, and N. J. Allen. 2018. "The Aging Astrocyte Transcriptome From Multiple Regions of the Mouse Brain." *Cell Reports* 22, no. 1: 269–285. https://doi.org/10.1016/j.celrep.2017.12.039.

Borodkina, A., A. Shatrova, P. Abushik, N. Nikolsky, and E. Burova. 2014. "Interaction Between ROS Dependent DNA Damage, Mitochondria and p38 MAPK Underlies Senescence of Human Adult Stem Cells." *Aging* 6, no. 6: 481–495. https://doi.org/10.18632/aging.100673.

Bussian, T. J., A. Aziz, C. F. Meyer, B. L. Swenson, J. M. van Deursen, and D. J. Baker. 2018. "Clearance of Senescent Glial Cells Prevents Tau-Dependent Pathology and Cognitive Decline." *Nature* 562, no. 7728: 578–582. https://doi.org/10.1038/s41586-018-0543-y.

Chuprin, A., H. Gal, T. Biron-Shental, et al. 2013. "Cell Fusion Induced by ERVWE1 or Measles Virus Causes Cellular Senescence." *Genes & Development* 27, no. 21: 2356–2366. https://doi.org/10.1101/gad.227512.113.

Clarke, L. E., S. A. Liddelow, C. Chakraborty, A. E. Münch, M. Heiman, and B. A. Barres. 2018. "Normal Aging Induces A1-like Astrocyte

10974652, 2025, 12, Downloaded from https://onlinelibrary.wiley.com/doi/10.1002/jcp.70118 by Yonsei University Med Library, Wiley Online Library on [22/01/2026]. See the Terms and Conditions (https://onlinelibrary.wiley.com/terms-and-conditions) on Wiley Online Library for rules of use; OA articles are governed by the applicable Creative Commons License

Reactivity." *Proceedings of the National Academy of Sciences* 115, no. 8: E1896–E1905. https://doi.org/10.1073/pnas.1800165115.

Cohen, J., and C. Torres. 2019. "Astrocyte Senescence: Evidence and Significance." *Aging cell* 18, no. 3: e12937. https://doi.org/10.1111/acel.12937.

Dodig, S., I. Čepelak, and I. Pavić. 2019. "Hallmarks of Senescence and Aging." *Biochemia Medica* 29, no. 3: 483–497. https://doi.org/10.11613/BM.2019.030501.

Etourneaud, L., A. Moussa, E. Rass, et al. 2021. "Lamin B1 Sequesters 53BP1 to Control Its Recruitment to DNA Damage." *Science Advances* 7, no. 35: eabb3799. https://doi.org/10.1126/sciadv.abb3799.

Harley, J., M. M. Santosa, C. Y. Ng, et al. 2024. "Telomere Shortening Induces Aging-Associated Phenotypes in hiPSC-Derived Neurons and Astrocytes." *Biogerontology* 25, no. 2: 341–360. https://doi.org/10.1007/s10522-023-10076-5.

Herbig, U., W. A. Jobling, B. P. C. Chen, D. J. Chen, and J. M. Sedivy. 2004. "Telomere Shortening Triggers Senescence of Human Cells Through a Pathway Involving ATM, p53, and p21(CIP1), but Not p16(INK4a)." *Molecular Cell* 14, no. 4: 501–513. https://doi.org/10.1016/s1097-2765(04)00256-4.

Hewitt, G., D. Jurk, F. D. M. Marques, et al. 2012. "Telomeres Are Favoured Targets of a Persistent DNA Damage Response in Ageing and Stress-Induced Senescence." *Nature Communications* 3: 708. https://doi.org/10.1038/ncomms1708.

Jaskelioff, M., F. L. Muller, J. H. Paik, et al. 2011. "Telomerase Reactivation Reverses Tissue Degeneration in Aged Telomerase-Deficient Mice." *Nature* 469, no. 7328: 102–106. https://doi.org/10.1038/nature09603.

Kang, C., Q. Xu, T. D. Martin, et al. 2015. "The Dna Damage Response Induces Inflammation and Senescence by Inhibiting Autophagy of GATA4." *Science* 349, no. 6255: aaa5612. https://doi.org/10.1126/science.aaa5612.

Kim, D., S. H. Yoo, G. B. Yeon, et al. 2024. "Senescent Astrocytes Derived From Human Pluripotent Stem Cells Reveal Age-Related Changes and Implications for Neurodegeneration." *Aging and Disease* 16, no. 3: 1709. https://doi.org/10.14336/AD.2024.0089.

Kim, Y. 2023. "The Impact of Altered Lamin B1 Levels on Nuclear Lamina Structure and Function in Aging and Human Diseases." *Current Opinion in Cell Biology* 85: 102257. https://doi.org/10.1016/j.ceb.2023.102257.

Kloc, M., A. Uosef, A. Subuddhi, J. Z. Kubiak, R. P. Piprek, and R. M. Ghobrial. 2022. "Giant Multinucleated Cells in Aging and Senescence-An Abridgement." *Biology* 11, no. 8: 1121. https://doi.org/10.3390/biology11081121.

Kohli, J., B. Wang, S. M. Brandenburg, et al. 2021. "Algorithmic Assessment of Cellular Senescence in Experimental and Clinical Specimens." *Nature Protocols* 16, no. 5: 2471–2498. https://doi.org/10.1038/s41596-021-00505-5.

Kumari, R., and P. Jat. 2021. "Mechanisms of Cellular Senescence: Cell Cycle Arrest and Senescence Associated Secretory Phenotype." *Frontiers in Cell and Developmental Biology* 9: 645593. https://doi.org/10.3389/fcell.2021.645593.

Lee, S., Y. Yu, J. Trimpert, et al. 2021. "Virus-Induced Senescence Is a Driver and Therapeutic Target in COVID-19." *Nature* 599, no. 7884: 283–289. https://doi.org/10.1038/s41586-021-03995-1.

Liddelow, S. A., K. A. Guttenplan, L. E. Clarke, et al. 2017. "Neurotoxic Reactive Astrocytes Are Induced by Activated Microglia." *Nature* 541, no. 7638: 481–487. https://doi.org/10.1038/nature21029.

Liu, H., D. Jia, A. Li, et al. 2013. "p53 Regulates Neural Stem Cell Proliferation and Differentiation via BMP-Smad1 Signaling and Id1." *Stem Cells and Development* 22, no. 6: 913–927. https://doi.org/10.1089/scd.2012.0370.

Lobanova, A., R. She, S. Pieraut, C. Clapp, A. Maximov, and E. L. Denchi. 2017. "Different Requirements of Functional Telomeres In Neural Stem Cells and Terminally Differentiated Neurons." *Genes & Development* 31, no. 7: 639–647. https://doi.org/10.1101/gad.295402.116.

López-Otín, C., M. A. Blasco, L. Partridge, M. Serrano, and G. Kroemer. 2023. "Hallmarks of Aging: An Expanding Universe." *Cell* 186, no. 2: 243–278. https://doi.org/10.1016/j.cell.2022.11.001.

Maestri, A., P. Garagnani, M. Pedrelli, C. E. Hagberg, P. Parini, and E. Ehrenborg. 2024. "Lipid Droplets, Autophagy, and Ageing: A Cell-Specific Tale." *Ageing Research Reviews* 94: 102194. https://doi.org/10.1016/j.arr.2024.102194.

Mah, L. J., A. El-Osta, and T. C. Karagiannis. 2010. "γH2AX: a Sensitive Molecular Marker of DNA Damage and Repair." *Leukemia* 24, no. 4: 679–686. https://doi.org/10.1038/leu.2010.6.

Matias, I., L. P. Diniz, I. V. Damico, et al. 2022. "Loss of lamin-B1 and Defective Nuclear Morphology Are Hallmarks of Astrocyte Senescence In Vitro and in the Aging Human Hippocampus." *Aging cell* 21, no. 1: e13521. https://doi.org/10.1111/acel.13521.

Melo Dos Santos, L., M. Trombetta-Lima, B. Eggen, and M. Demaria. 2024. "Cellular Senescence in Brain Aging and Neurodegeneration." *Ageing Research Reviews* 93: 102141. https://doi.org/10.1016/j.arr.2023.102141.

Di Micco, R., V. Krizhanovsky, D. Baker, and F. d'Adda di Fagagna. 2021. "Cellular Senescence in Ageing: From Mechanisms to Therapeutic Opportunities." *Nature Reviews Molecular Cell Biology* 22, no. 2: 75–95. https://doi.org/10.1038/s41580-020-00314-w.

Nousis, L., P. Kanavaros, and A. Barbouti. 2023. "Oxidative Stress-Induced Cellular Senescence: Is Labile Iron the Connecting Link?" *Antioxidants (Basel, Switzerland)* 12, no. 6: 1250. https://doi.org/10.3390/antiox12061250.

Oguma, Y., N. Alessio, D. Aprile, et al. 2023. "Meta-Analysis of Senescent Cell Secretomes to Identify Common and Specific Features of the Different Senescent Phenotypes: A Tool for Developing New Senotherapeutics." *Cell Communication and Signaling* 21, no. 1: 262. https://doi.org/10.1186/s12964-023-01280-4.

Pascolo, E., C. Wenz, J. Lingner, et al. 2002. "Mechanism of Human Telomerase Inhibition by BIBR1532, a Synthetic, Non-Nucleosidic Drug Candidate." *Journal of Biological Chemistry* 277, no. 18: 15566–15572. https://doi.org/10.1074/jbc.M201266200.

Sacco, A., L. Belloni, and L. Latella. 2021. "From Development to Aging: The Path to Cellular Senescence." *Antioxidants & Redox Signaling* 34, no. 4: 294–307. https://doi.org/10.1089/ars.2020.8071.

Salminen, A., A. Kauppinen, and K. Kaarniranta. 2012. "Emerging Role of NF-κB Signaling in the Induction of Senescence-Associated Secretory Phenotype (SASP)." *Cellular Signalling* 24, no. 4: 835–845. https://doi.org/10.1016/j.cellsig.2011.12.006.

Simmnacher, K., F. Krach, Y. Schneider, et al. 2020. "Unique Signatures of Stress-Induced Senescent Human Astrocytes." *Experimental Neurology* 334: 113466. https://doi.org/10.1016/j.expneurol.2020.113466.

Spilsbury, A., S. Miwa, J. Attems, and G. Saretzki. 2015. "The Role of Telomerase Protein Tert in Alzheimer's Disease and in Tau-Related Pathology In Vitro." *Journal of Neuroscience* 35, no. 4: 1659–1674. https://doi.org/10.1523/JNEUROSCI.2925-14.2015.

Tavares, G., M. Martins, J. S. Correia, et al. 2017. "Employing An Open-Source Tool to Assess Astrocyte Tridimensional Structure." *Brain Structure and Function* 222, no. 4: 1989–1999. https://doi.org/10.1007/s00429-016-1316-8.

Tomita, K., J. Aida, N. Izumiyama-Shimomura, et al. 2018. "Changes in Telomere Length With Aging in Human Neurons and Glial Cells Revealed by Quantitative Fluorescence In Situ Hybridization Analysis." *Geriatrics & Gerontology International* 18, no. 10: 1507–1512. https://doi.org/10.1111/ggi.13500.

Vera, E., N. Bosco, and L. Studer. 2016. "Generating Late-Onset Human iPSC-Based Disease Models by Inducing Neuronal Age-Related Phenotypes Through Telomerase Manipulation." *Cell Reports* 17, no. 4: 1184–1192. https://doi.org/10.1016/j.celrep.2016.09.062.

10974652, 2025, 12, Downloaded from https://onlinelibrary.wiley.com/doi/10.1002/jcp.70118 by Yonsei University Med Library, Wiley Online Library on [22/01/2026]. See the Terms and Conditions (https://onlinelibrary.wiley.com/terms-and-conditions) on Wiley Online Library for rules of use; OA articles are governed by the applicable Creative Commons License

Yan, J., S. Chen, Z. Yi, et al. 2024. "The Role of p21 in Cellular Senescence and Aging-Related Diseases." *Molecules and Cells* 47, no. 11: 100113. https://doi.org/10.1016/j.mocell.2024.100113.

Yeon, G. B., B. M. Jeon, S. H. Yoo, et al. 2023. "Differentiation of Astrocytes With Characteristics of Ventral Midbrain From Human Embryonic Stem Cells." *Stem Cell Reviews and Reports* 19, no. 6: 1890–1906. https://doi.org/10.1007/s12015-023-10536-y.

Yeon, G. B., W. H. Shin, S. H. Yoo, et al. 2021. "NFIB Induces Functional Astrocytes From Human Pluripotent Stem Cell-Derived Neural Precursor Cells Mimicking In Vivo Astrogliogenesis." *Journal of Cellular Physiology* 236, no. 11: 7625–7641. https://doi.org/10.1002/jcp.30405.

Zhang, W., H. S. Sun, X. Wang, A. S. Dumont, and Q. Liu. 2024. "Cellular Senescence, DNA Damage, and Neuroinflammation in the Aging Brain." *Trends in Neurosciences* 47, no. 6: 461–474. https://doi.org/10.1016/j.tins.2024.04.003.

Supporting Information

Additional supporting information can be found online in the Supporting Information section.
Supporting Figure Kim et al R2. Supporting Table Kim et al Re1.

10974652, 2025, 12, Downloaded from https://onlinelibrary.wiley.com/doi/10.1002/jcp.70118 by Yonsei University Med Library, Wiley Online Library on [22/01/2026]. See the Terms and Conditions (https://onlinelibrary.wiley.com/terms-and-conditions) on Wiley Online Library for rules of use; OA articles are governed by the applicable Creative Commons License